CrossMark

Iron oxide/PAMAM nanostructured hybrids: combined computational and experimental studies

Marco Agostino Deriu[1] · Laura Madalina Popescu[2] ·
Maria Francesca Ottaviani[3] · Andrea Danani[1] ·
Roxana Mioara Piticescu[2]

Abstract Recent studies in the field of iron oxide–dendrimer hybrids showed an increased potential of these materials to be used in diagnosis, monitoring, targeting, and therapy of cancer. The aim of this paper is to investigate the nature of interactions between iron oxide nanoparticles and polyamidoamine (PAMAM) dendrimers using computational and experimental techniques, namely molecular dynamics (MD) and electron paramagnetic resonance (EPR). Hybrid nanostructures based on iron oxide and PAMAM dendrimers were prepared in one-step synthesis route, using hydrothermal method at high pressure (40–100 atm). The interaction between dendrimers and iron oxide nanoparticles was predicted at specific temperature, pH, and pressure conditions. The same conditions were applied for hydrothermal synthesis. High-resolution transmission electron microscopy revealed the formation of magnetite (MAG) through hydrothermal reaction at 100 atm, starting only from iron (III) chloride. A possible explanation could be the variation of the fugacity value of oxygen under high-pressure conditions, which leads to diffusion-controlled reaction and to transformation of haematite into MAG. EPR parameter, namely linewidth, was exploited to evaluate the type of interactions from iron oxide–PAMAM hybrids, due to its dependence on spin–spin relaxation time and spin–lattice interactions. As a conclusion, MD indicated the existence of electrostatic interactions between PAMAM and iron oxide. In accordance with in silico results, EPR analysis suggested that MAG is not entrapped in PAMAM structure and the interactions between organic and inorganic components take place at dendrimer's surface. A good agreement between MD simulations and experimental results was observed.

Marco Agostino Deriu and Laura Madalina Popescu have equally contributed to this study.

Electronic supplementary material The online version of this article (doi:10.1007/s10853-015-9509-8) contains supplementary material, which is available to authorized users.

✉ Andrea Danani
andrea.danani@idsia.ch

✉ Roxana Mioara Piticescu
roxana@imnr.ro

Marco Agostino Deriu
marco.deriu@idsia.ch

Laura Madalina Popescu
mpopescu@imnr.ro

Maria Francesca Ottaviani
maria.ottaviani@uniurb.it

[1] IDSIA, Dalle Molle Institute for Artificial Intelligence, Centro Galleria 2, 6928 Manno, Switzerland

[2] National R&D Institute for Non-ferrous and Rare Metals, 102 Biruintei Blvd, 077145 Pantelimon, Ilfov, Romania

[3] Department of Earth, Life and Environmental Sciences (DiSTeVA), University of Urbino "Carlo Bo", Via Ca' le Suore 2/4, 61029 Urbino, Italy

Introduction

Nanoparticles (NPs) have become very attractive for their applications in different fields, comprising biology, medicine, drug delivery systems, engineering, electronics, etc. [1, 2]. Several previous studies have explored the possibility to combine NPs with dendrimers and other polymers to build hybrid nanoscale structures for various purposes [3–6]. The dendrimer–nanoparticle conjugation can be

obtained via two approaches: the physical encapsulation of particles in the internal cavity of a dendrimer, and the chemical formation of dendrimer branches around the inorganic core [7–16]. For example, dendrimer-grafted magnetite (MAG) nanoparticles were synthesized in order to improve the efficiency of coating formation on the surface of MAG nanoparticles. In particular, polyamidoamine (PAMAM) dendrimers were built on the surface of amine-functionalized MAG nanoparticles [7].

An interesting characteristic of dendrimers is that they can be covalently linked with several ligands, dyes, and drugs, thus providing a platform for the specific targeting, imaging, and treatment of cancer. In this context, dendrimer-based organic/inorganic hybrids have been considered for targeting and imaging tumour in animal models of human cancer [7, 17–19]. For example, magnetic NPs (in particular ferric oxide, Fe_2O_3) were modified with different generations of PAMAM dendrimers and mixed with anti-sense surviving oligodeoxynucleotides for applications in cancer therapy and MRI diagnosis [8–10, 20]. In a recent study, iron (II, III) oxide, Fe_3O_4, has been functionalized with polyelectrolyte (polystyrene sulfonate sodium salt, PSS) and PAMAM generation 5 (G5) dendrimers [21]. In detail, dendrimers were pre-functionalized with folic acid (FA) and fluorescein isothiocyanate (FI) moieties (G5.NH2-FI-FA) on the surface of iron oxide NPs using the LbL self-assembly technique. The formed FI- and FA-functionalized iron oxide NPs displayed very high specific binding affinity to cancer cells. Iron oxide NPs have been also synthesized in the presence of carboxylated PAMAM dendrimers G4.5 [12]. The electrostatic interaction of negatively charged carboxylated PAMAM dendrimers with positively charged iron oxide NPs is considered to play an important role for the stabilization of the NPs [9], whereas PAMAM dendrimers with other different functionalities (–NH2, –OH) might not be able to stabilize iron oxide NPs, indicating the role of electrostatic interaction for the NP stabilization [22].

Taking into account the current state of the art briefly described above, the present work is focused on hybrid nanosystems composed of MAG and PAMAM dendrimers functionalized with succinamic acid groups on its surface, prepared in a single step in high-pressure conditions (hydrothermal procedure).

The aim of this paper is to investigate the nature of interactions between MAG NPs and PAMAM dendrimers, in hydrothermal conditions, using computational and experimental techniques.

Computational simulations to predict the interactions between organic and inorganic components at high pressures and low temperatures were validated by experimental approaches in hydrothermal conditions.

Methodology

In this work, molecular modelling has been employed to investigate the interaction mechanism between PAMAM dendrimers and MAG particles, at high pressure values (100 atm). Simulation outcomes served as a starting point for identifying dendrimer types with the highest affinity for MAG nanoparticles. Those dendrimers have been then chosen for hydrothermal synthesis of hybrid nanostructured compound. Commercially available PAMAM dendrimers decorated with succinamic acid groups were specially selected as they are soluble in water and may easily interact with Fe^{3+} ions through carboxylic groups of succinamic acid.

Simulation models were validated by hydrothermal synthesis experiments at 100 atm and 40 °C. MAG/dendrimer hybrids' structural properties have been also investigated by high-resolution transmission electron microscopy (HRTEM) and electron paramagnetic resonance (EPR) experimental techniques. A detailed description of materials and methods employed in this paper is reported in the following paragraphs.

Computational method

MD is powerful as a virtual microscope to investigate structural characteristics and interaction dynamics at molecular level [23–26], and it has been extensively used to model dendrimer systems [19–22, 27–31].

The aim of the molecular dynamics (MD) studies was to predict the interaction between dendrimer and MAG particles at specific temperature, pH, and pressure conditions, using atomistic modelling. To this aim, we compared two types of dendrimer differing in terminal groups exposed to the solvent: (i) the 1,4-diaminobutane core poly(amidoamine) (PAMAM) with NH2 terminal groups, which is soluble in methanol and insoluble in water, and (ii) 1,4-diaminobutane core poly(amidoamine) decorated with succinamic acid (PAMAM-SAHs), which has anionic surface groups, and typical carboxylic acid reactivity and is water soluble. For each dendrimer type, four generations (from G1 to G4) were considered. Linear formulas of each type of dendrimer are presented in Table 1.

Dendrimer models were built, parameterized, and refined according to [13–16]. A refined three dimensional atoms' arrangement was obtained by employing as a working platform the Dendrimer Building Toolkit (DBT) [27]. Each PAMAM dendrimer was considered as made of three main hyperbranched residue types: AAA (dendrimer core), BBB (dendrimer branch), and CCC (dendrimer terminal). A second terminal type, namely SUC, constituted by a CCC (the PAMAM amine terminal) attached to a

Table 1 Linear formulas of modelled PAMAM dendrimers

Sample name	Formula	Dendrimer generation	Terminal groups
PAMAM G1	$NH_2(CH_2)_4NH_2$:G=1 dendri PAMAM$(NH_2)_8$	1	8
PAMAM G2	$NH_2(CH_2)_4NH_2$:G=2 dendri PAMAM$(NH_2)_{16}$	2	16
PAMAM G3	$NH_2(CH_2)_4NH_2$:G=3 dendri PAMAM$(NH_2)_{32}$	3	32
PAMAM G4	$NH_2(CH_2)_4NH_2$:G=4 dendri PAMAM$(NH_2)_{64}$	4	64
PAMAM-SAH G1	$NH_2(CH_2)_4NH_2$:G=1 dendri PAMAM$(NHCOCH_2CH_2COOH)_8$	1	8
PAMAM-SAH G2	$NH_2(CH_2)_4NH_2$:G=2 dendri PAMAM$(NHCOCH_2CH_2COOH)_{16}$	2	16
PAMAM-SAH G3	$NH_2(CH_2)_4NH_2$:G=3 dendri PAMAM$(NHCOCH_2CH_2COOH)_{32}$	3	32
PAMAM-SAH G4	$NH_2(CH_2)_4NH_2$:G=4 dendri PAMAM$(NHCOCH_2CH_2COOH)_{64}$	4	64

succinic group $HOOC–(CH_2)_2–COOH$ was defined. A dedicated in-house code has been employed for building the decorated dendrimer starting from PAMAM obtained by DBT.

The general Amber force field (GAFF) [32, 33] has been employed for force field parameters.

Force fields define a set of parameters for different types of atoms, chemical bonds, dihedral angles, etc. The typical parameter set includes values for atomic mass, van der Waals radius, and partial charge for individual atoms, and equilibrium values of bond lengths, bond angles, and dihedral angles for pairs, triplets, and quadruplets of bonded atoms, and values corresponding to the effective spring constant for each potential.

Partial charges were calculated by the restrained electrostatic potential (RESP) fitting method at the HF/6-31G* level of theory using Gaussian09 via the RESP ESP charge Derive Server (R.E.D.Server) [34–37]. Simulations have been set up on the basis of the parameters that will be considered in experimental approach: high pressure (100 atm) and pH 10. Hence, dendrimer models and relative force field were built by considering completely deprotonated structures (e.g. non-protonated amine terminals NH_2 and carboxylate terminals COO–).

The MAG atomic coordinates were obtained by Crystallography Open Database (COD ID: 1011084). The unit cell had a size of 8.39 Å, composed of 28 atoms, 12 irons, and 16 oxygens, resulting in an oxygen/iron ratio of 4:3. A spherical MAG particle, with a diameter of roughly 4 nm, was created starting from COD data of a MAG super-cell of $5 \times 5 \times 5$ nm. The clay force field [38] have been employed for defining MAG particle atom types and non-bonded topology (vdW and Coulomb). Partial charge optimization was carried out by GULP suite [39–41] following the Rappe and Goddard's charge equilibration method [42].

Bonded topology for the MAG particle has been defined as an elastic network connected by harmonic potentials. Elastic network parameters have been refined, starting from

the clay force field, by an iterative Boltzmann inversion (IBI) procedure which allowed us to define a set of bond parameters (force constant k, and reference length r_0) able to reproduce a reasonable distribution of MAG atomic fluctuations under thermal motion during the simulated conditions. The application of the IBI procedure, implemented following the procedure described in [43–46], allowed to avoid position restraints on MAG particles during MD simulations, taking into account molecule/surface interactions [47, 48]. Dendrimer models have been employed to set up eight molecular systems (four generations for PAMAM and PAMAM-SAHs, respectively), each constituted by one dendrimer and one MAG particle positioned at an initial distance of about 1 nm. Dendrimer- and MAG-based systems were then immersed in a box of TIP3P water molecules [49]. The dimension of each simulation triclinic box was chosen in order to ensure at least 1 nm solvation shell around the solute (dendrimer + MAG). Each system was first minimized by steepest descent energy minimization algorithm followed by a preliminary position-restrained MD of about 1 ns in isothermal–isobaric ensemble (310 K and 100 atm). A further production MD (none restraint applied) in the NVT ensemble at 310 K was carried out for 50 ns leaving the dendrimer and the MAG particle free to fluctuate under thermal motion and eventually interact. All simulations discussed in this work were carried out by GROMACS [50–52]. The visual molecular dynamics (VMD) [53] package was employed for the visual inspection of the simulated systems. Dedicated GROMACS tools were used for a quantitative analysis in terms of root-mean-square deviation (RMSD), root-mean-square fluctuation (RMSF), solvent-accessible surface (SAS) [54], contact surface, and radius of gyration (R_g). On a time interval characterized by a stable contact surface between dendrimer and MAG (i.e. the last 10 ns of each simulation), we have estimated the binding energy by the molecular mechanics Poisson–Boltzmann surface area (MM/PBSA), widely employed to analyse biomolecular interactions [55]. MM/PBSA data

have been used to obtain insights into the nature of the dendrimer–MAG interaction, in particular in terms of comparison between PAMAM and PAMAM-SAHs.

Experimental details

PAMAM dendrimers with succinamic acid surface groups (generations G4 and G2, respectively) were purchased as solution 10 wt% in H_2O from Sigma-Aldrich (www.sigmaaldrich.com) and used as received. Iron (III) chloride hexahydrate, p.a. (Merck) solid salt, was dissolved in water and used as solution 20 wt% in H_2O. Ammonia solution 25 % (Chimreactiv S.R.L.) was used as a mineralizing agent. Based on MD results and dendrimers' solubility in water, PAMAM-SAH G4 dendrimer was selected for hydrothermal synthesis and characterization of hybrid organic–inorganic nanoparticles. Hence, investigated hybrid nanostructures were constituted by MAG NPs and PAMAM-SAH G4. PAMAM-SAH G2 was also considered for hybrid synthesis, as a comparison term. Linear formulas of these dendrimers are presented in Table 1. Hydrothermal synthesis parameters are presented in Table 2.

Hydrothermal synthesis of hybrid nanostructures

Iron (III) chloride hexahydrate and ammonia solutions were vigorously mixed until a strong alkaline suspension (pH 10) was obtained. PAMAM-SAH dendrimer (solution 10 wt% in H_2O) was further added to inorganic suspension, and the mixture was transferred in Teflon vessel of a closed autoclave (SAM, Romania) and endorsed with cooling system, for hydrothermal reaction at 40 °C and high pressure of 40 and 100 atm, respectively. Pressure was created inside the reaction system using argon gas. The resulted suspensions based on MAG–PAMAM nanostructures were lyophilized at −50 °C using a Martin Christ Alpha 1–2 LD Plus freeze dryer.

For comparative reasons, MAG nanoparticles were also prepared in aqueous solution starting from iron (III) chloride hexahydrate and ammonia, in the same conditions as nanostructured organic–inorganic hybrid. MAG nanoparticles were obtained after freeze drying at −50 °C of the resulted suspension. Both nanostructured MAG–PAMAM

hybrid systems and MAG nanoparticles were characterized using HRTEM and EPR techniques.

Characterization

Structural properties, thermal behaviour, and morphology of iron oxide–PAMAM hybrid nanostructures were investigated using Fourier-transformed Infrared spectroscopy (FT-IR), EPR, thermal gravimetry (TGA), differential scanning calorimetry (DSC), and HRTEM analyses. FT-IR, TGA, and DSC results were presented elsewhere [3].

(a) *HRTEM characterization* Samples were dispersed in ethylic alcohol, and a drop of the as-resulted suspension was deposited on a TEM copper grid coated with a thin amorphous carbon film with holes. Morphostructural characterization of the samples presented in Table 2 was investigated using high-resolution transmission electron microscope Tecnai F30, G2S Twin (1 Å line resolution)—FEI Company. Examination of the nanoparticles' morphology was performed at 300 kV.

(b) *EPR characterization* The EPR spectra were recorded for the samples presented in Table 2, in the temperature range between 100 and 350 K, by means of an EMX-Bruker spectrometer operating at X band (9.5 GHz) and interfaced with a PC (software from Bruker for handling and analysis of the EPR spectra). The temperature was controlled with a Bruker ST3000 variable-temperature assembly cooled with liquid nitrogen. The reproducibility of the results was controlled by repeating the EPR analysis three times in the same experimental conditions for each sample. All the spectra were performed in the same instrumental conditions to permit a comparison of the absolute intensity among the different samples. These conditions, termed "standard", are detailed in the following: (i) receiver gain 6.32×10^2, (ii) modulation amplitude 3 G, (iii) time constant 10.24 ms, (iv) conversion time 40.96 ms, (v) resolution 2048 points, (vi) number of scans 10, and (vii) EPR tube size 2 mm internal.

Table 2 Hydrothermal synthesis parameters

Sample name	Type of nanostructure	Mass ratio[a]	Synthesis parameters
MAG	Magnetite nanoparticles	–	40 °C/3 h/100 atm
MAG G2 40 atm	Magnetite–PAMAM-SAH G2 hybrid	1:1	40 °C/3 h/40 atm
MAG G2 100 atm	Magnetite–PAMAM-SAH G2 hybrid	1:1	40 °C/3 h/100 atm
MAG G4 100 atm	Magnetite–PAMAM-SAH G4 hybrid	1:1	40 °C/3 h/100 atm

[a] Iron oxide:PAMAM theoretically calculated mass ratio

Results and discussion

Computational analysis

Along the overall MD simulation, the dendrimer–MAG binding dynamics can be reasonably divided into three phases by observing the contact surface plots shown in Fig. 1: (1) a first phase (0–20 ns) characterized by the dendrimer's nearest position and non-covalent binding of the MAG nanoparticle, (2) a transition phase (20–40 ns) in which the contact surface may still increase due to conformational changes of the dendrimer, and (3) a third phase in which the contact surface is stabilized (40–50 ns). In this phase, also dendrimer conformational properties, such as the radius of gyration (R_g), reached a reasonable stability in all cases, as shown in Supporting Information section S1.1. As expected, the average PAMAM-SAH R_g value was always higher than the PAMAM R_g (S1.1—Figs. S.1, S.2) if comparing the same generation. In detail, as the number of succinic terminals increases, the dendrimer structure loses compactness due to the repulsion of negative succinic terminals on the surface, similarly to the PAMAM dendrimer at a neutral pH [31]. In Fig. 1, the relationship

between dendrimer generation and area of the contact surface is presented. In the case of PAMAM dendrimer, the area of the contact surface depends directly on the dendrimer generation, while for PAMAM-SAH no dependence is observed. In particular, the PAMAM-SAH G2 showed the highest contact surface.

A visual inspection through VMD helped in examination of the contact between dendrimer and NPs (Fig. 2, section S1.2). In particular, from the indicative picture shown in the left panel of Fig. 2, it can be noticed that the mode of binding between PAMAM and MAG NP is different from the one between PAMAM-SAHs and MAG NP. A detailed explanation of the binding modes characterizing PAMAM and PAMAM-SAH dendrimers is provided in Supporting Information section S1.2.

This binding mode may be also quantified by the calculation of the radial distribution function (RDF) of dendrimer atoms with respect to the MAG surface (Fig. 2). Atomic distribution for all generations of PAMAM dendrimers is picked at a distance of about 0.5 nm from the MAG surface, decreasing quickly for higher distances. A slightly wider distribution is found for PAMAM G3 and G4. RDF curves calculated for PAMAM-SAH dendrimers show an interesting dependence on dendrimer size. G3 and G4 RDF curves for PAMAM-SAH clearly indicate that a large part of the dendrimer does not interact with MAG NPs (the contact surface between MAG and dendrimer is lower), as clearly shown in Fig. 2.

The different binding mode emphasized for the decorated (PAMAM-SAHs) and not decorated PAMAM dendrimers reflects the different nature of dendrimer/ MAG interaction. Using the MM/PBSA approach, we have calculated the binding energy during the last 10 ns of each simulation (Fig. 3). The binding energy has been calculated by considering van der Waals, electrostatic, non-polar, and polar contributions. In all cases, given a defined size of the NP ($\sim$4 nm in this study), the dendrimer/MAG affinity rises proportionally with the dendrimer generation. Moreover, the PAMAM-SAH dendrimers have shown a much higher increase of the binding energy resulting in a value of about -2.0 MJ/mol for G4. While, for non-decorated PAMAM, it is possible to relate the slight increase of affinity to the increase of the contact area, this relationship may not be inferred for PAMAM-SAHs.

Data coming from MM/PBSA calculations have indicated that dendrimer/MAG affinity may be dependent, as expected, on the dendrimer size. Moreover, our data have also highlighted how the interaction between PAMAM-SAHs and MAG is mainly driven by the electrostatic contribution, whereas, in case of non-decorated PAMAM, the vdW contribution drives the interaction. PAMAM-
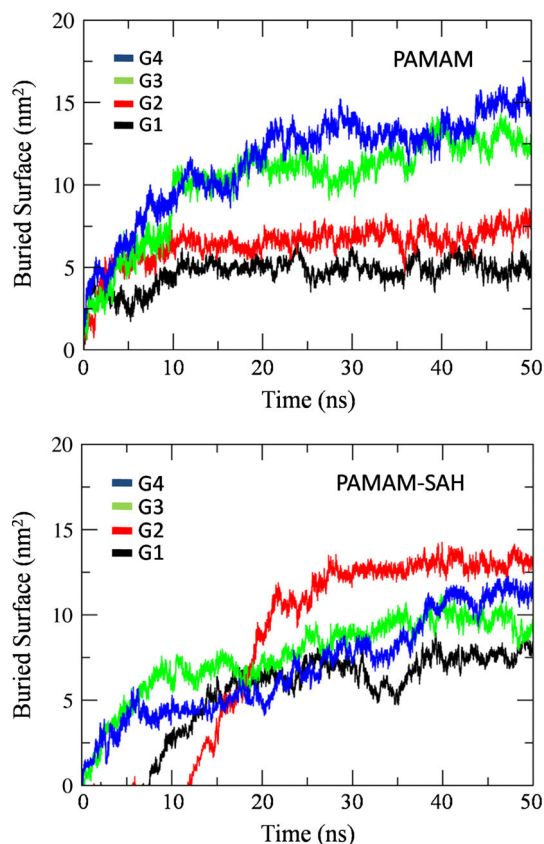

Fig. 1 Dendrimer–MAG contact surface throughout the MD simulation. A reasonably stable contact surface is observed in the last 10 ns for all simulations

Fig. 2 Normalized radial distribution function versus dendrimer atoms' distance from MAG surface (nm). In PAMAM-SAHs G3 and G4, a wide part of the dendrimer remains far from the MAG surface and free to eventually bind other MAG nanoparticles. On the left, an MD snapshot taken in the last 10 ns of the MD simulation for G4 PAMAM and PAMAM-SAHs. Water molecules are not shown in the picture
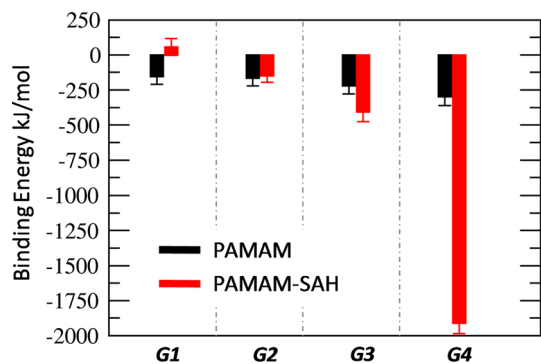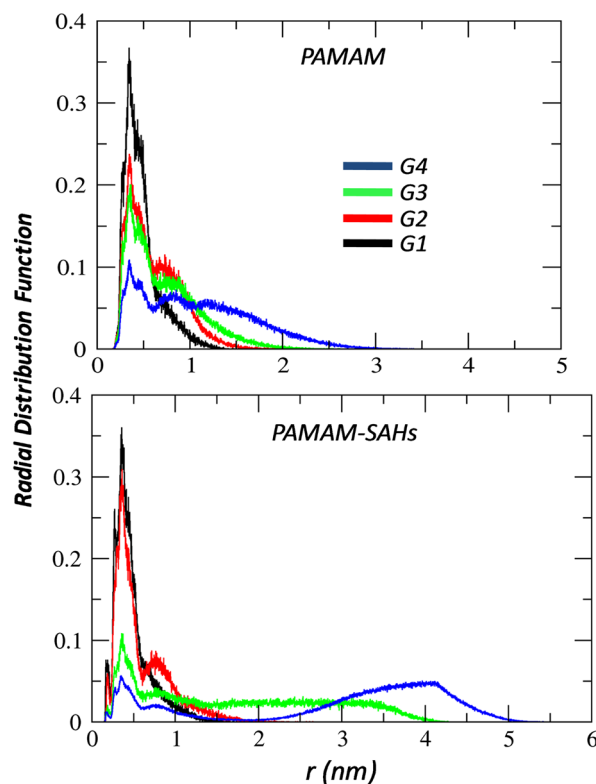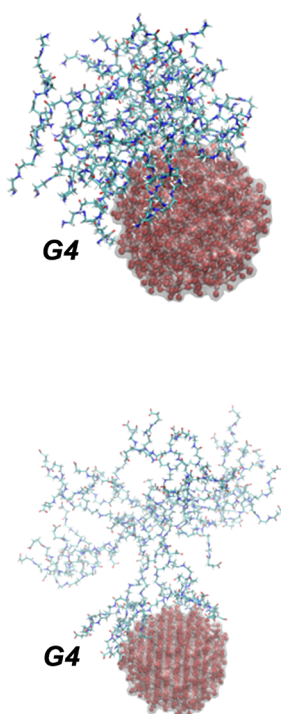

Fig. 3 MM/PBSA binding energy calculated for different generations of PAMAM and PAMAM-SAH dendrimers. Affinity of the PAMAM dendrimers for MAG increases slightly moving from G1 to G4. Binding energy is mainly related to the increase of the contact surface. PAMAM-SAH affinity is mainly driven by the electrostatic contribution. The number of succinic groups exposed in the dendrimer outer surface is responsible for the affinity increase much more than the contact surface

Fig. 4 Dendrimer/MAG binding energy decomposition over the interaction energy contributions

SAHs, characterized by negatively charged succinamic acid surface groups at high pH, have shown a much higher affinity for MAG NPs. Binding energy decomposition (Fig. 4) clearly highlighted a change in main players contributing the binding energy. While the binding energy is mainly dominated by the vdW contribution for PAMAM, electrostatics is almost totally responsible in the case of PAMAM-SAHs, in particular for higher generations where
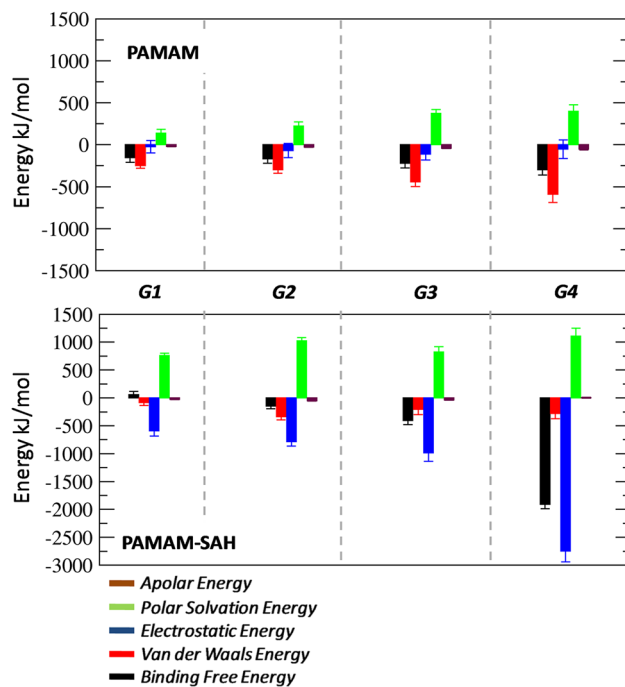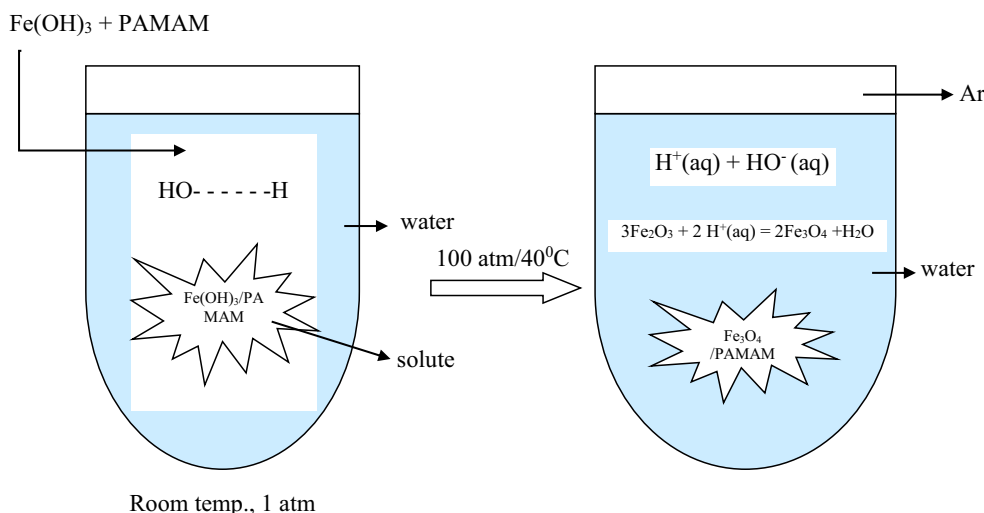
the number of terminal succinamic groups overcome a certain threshold (as in the case of G3 and G4 PAMAM-SAHs).

Scheme 1 Possible mechanism of hybrid organic–inorganic nanostructure formation

Fe(OH)$_3$ + PAMAM

HO- - - - -H

Fe(OH)$_3$/PAMAM

water

solute

Room temp., 1 atm

100 atm/40^{0}C

H$^+$(aq) + HO$^-$ (aq)

3Fe$_2$O$_3$ + 2 H$^+$(aq) = 2Fe$_3$O$_4$ +H$_2$O

Fe$_3$O$_4$/PAMAM

Ar

water

Experimental

Hydrothermal synthesis in high-pressure conditions

Inorganic–organic nanohybrids have been prepared by hydrothermal method at high pressure, with several advantages briefly mentioned as follows:

(i) low energy developed by applying pressure (for a liquid phase, the same energy is involved on five units for the temperature scale than on 4000 units for the pressure scale);

(ii) negative ΔV value [$\Delta V = \Sigma(V/Z)(j)-\Sigma(V/Z)(i)$], where i indicates the *precursor* and j the *product*;

(iii) improvement of the chemical reactivity. When pressure is imposed, the distance between inorganic nanoparticles and PAMAM decreases, and weak physical bonds appear between terminal groups of dendrimer and Fe^{3+} ions.

However, little is known about the reaction mechanism of MAG formation in hydrothermal conditions, starting from iron (III) chloride hexahydrate.

The lowering of the surface activity of adsorbed gas molecules is dependent on pressure increase and is more evident in the case of non-polar gases like Ar or O$_2$ [56].

In order to have a combination of Fe^{3+} and Fe^{2+} ions present, MAG requires at least a moderate fugacity value of oxygen (fO$_2$) [57]. At a working pressure of 100 atm, water dissociation determined by pressure and solutes (amorphous iron hydroxide and PAMAM dendrimer) may appear [58]:

$$H_2O \leftrightarrow H_{aq}^+ + HO_{aq}^-.$$
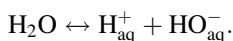
H$^+$(aq) could determine the reduction of Fe^{3+} to Fe^{2+} and the formation of MAG [59].

Moreover, in high-pressure conditions (40–100 atm), reaction kinetics are controlled by diffusion of gases to and from haematite–magnetite [60].

A possible explanation of the MAG formation could be that the pressure inside the system was created by Ar gas in aqueous medium, as presented in Scheme 1. Solubility of Ar in water is very low at working pressure [61]. Thus, at the liquid–gas surface, the probability to form hydrogen bonds with the gas is reduced. The surface tension is increased due to the fact that water molecules from the surface are attracted inside the water volume by the remaining stronger hydrogen bonds [56].

$$FeCl_3 + 3NH_3 + 3H_2O = Fe(OH)_3+3NH_4Cl$$
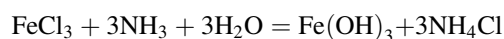
Characterization

(a) *HRTEM characterization* Different morphologies of MAG NP alone and nanohybrids MAG/PAMAM-SAHs are revealed in Fig. 5.

(a) HRTEM micrograph of MAG nanoparticles alone (Fig. 5a) shows typical morphology of hydrothermally prepared nanostructures with crystallite size ranging between 2 and 5 nm. Round-shaped nanoparticles are formed.

(b) In the case of dendrimer G2, small crystallites of 6–15 nm, as well as aggregates consisting of crystallites with 3 nm in size, can be observed (Fig. 5b).

(c) The presence of MAG nanoparticles in hybrid structures with G4 PAMAM-SAH was proved by calculated interplanar distance (2.53 Å) and associated Miller index (311). Crystallite size of MAG in this type of hybrid is about 3 nm (Fig. 5c).

Fig. 5 HRTEM images of **a** magnetite nanoparticles, **b** hybrid nanostructures with PAMAM-SAH G2, and **c** hybrid nanostructures with PAMAM-SAH G4

(a) MAG NP

(b) MAG-PAMAM-SAH G2

(c) MAG-PAMAM-SAH G4
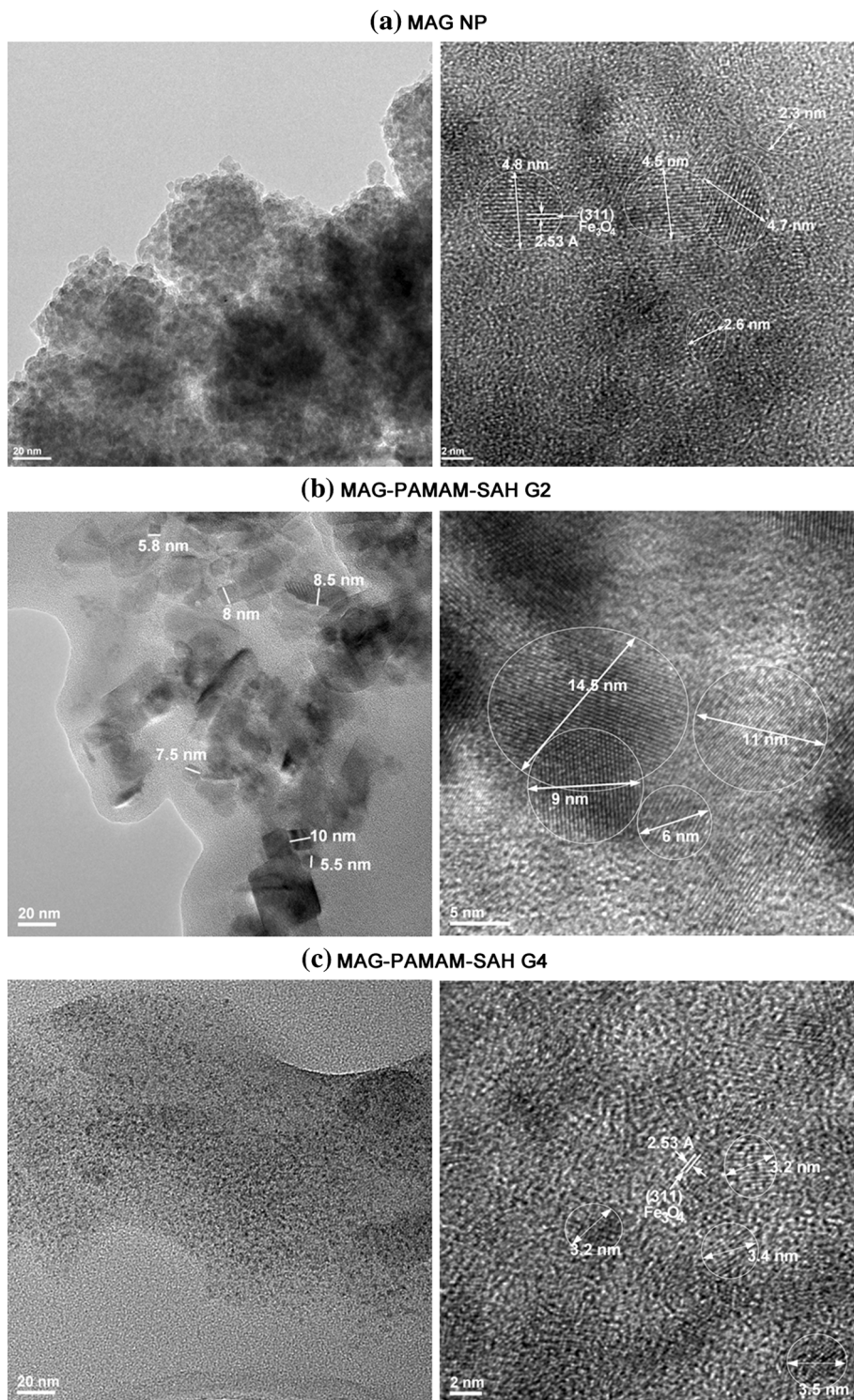
Unfortunately, HRTEM images cannot indicate if MAG NPs are entrapped or not in dendrimer's cage. For a better understanding of this aspect, EPR analysis was performed.

(b)   *EPR characterization* EPR spectra were recorded in order to study the nature of interactions between MAG and PAMAM dendrimer.

It is well known that MAG is a ferrous-ferric oxide, containing Fe^{2+} and Fe^{3+} in its structure. However, Fe^{2+} ions are not involved in EPR absorption, but their interaction with Fe^{3+} ions influences the characteristics of the absorption lines, according to Castner and coworkers [62]. Thus, the EPR investigation discussed in this paper refers

to Fe^{3+} and their interaction with PAMAM-SAH dendrimer.

Some examples of the room-temperature (298 K) EPR spectra (normalized in height) obtained for Fe_3O_4 NPs alone (MAG) and MAG–PAMAM-SAH hybrid structures (samples presented in Table 2) are shown in Fig. 6. The room-temperature spectra of the MAG NPs interacting with the dendrimer structure are constituted by a single line at approximately $g = 2.03$ (measured using as a reference the 2,2-diphenyl-1-picrylhydrazyl, DPPH radical with $g = 2.0036$). At g around 2, signal is usually attributed to those ions which interact by super-exchange interaction. The $g = 2.03$ value is in good agreement with the one reported in the literature for α-Fe_2O_3 NPs [63].

EPR parameters which characterize EPR spectra are gyromagnetic factor (g), absorption intensity (I), linewidth (ΔH_{pp}), splitting type, and coupling constant. Linewidth enables to evaluate the type of interactions from the studied hybrids, due to its dependence on spin–spin relaxation time and spin–lattice interactions.

EPR parameters such as absorption line intensity, estimated from double integration of the spectra, and the linewidth (ΔH_{pp}) of the EPR absorption profiles of the MAG NPs and MAG–PAMAM-SAH hybrid structures (samples presented in Table 2) are depicted in Fig. 7.

The dendrimer structure affects the EPR parameters of the hybrid nanostructures. The decrease of the intensity with the increase of pressure and dendrimer generation (Fig. 7a) could be explained by the interactions with vicinal SAH groups (mainly electrostatic, as shown by computational simulations) which suppressed the super-exchange interaction between Fe^{3+} and Fe^{2+} ions.
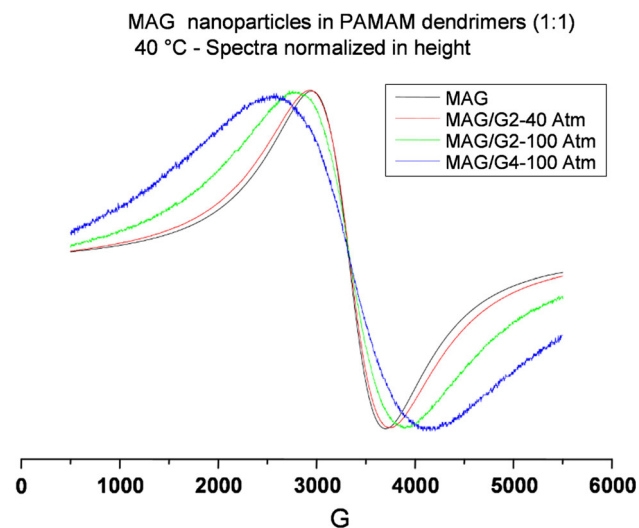

Fig. 6 Examples of room-temperature (298 K) EPR spectra (normalized in height) obtained for MAG NPs alone and embedded into PAMAM dendrimer structure (1:1 ratio) at different generations (G2, G4). The preparation conditions are also indicated
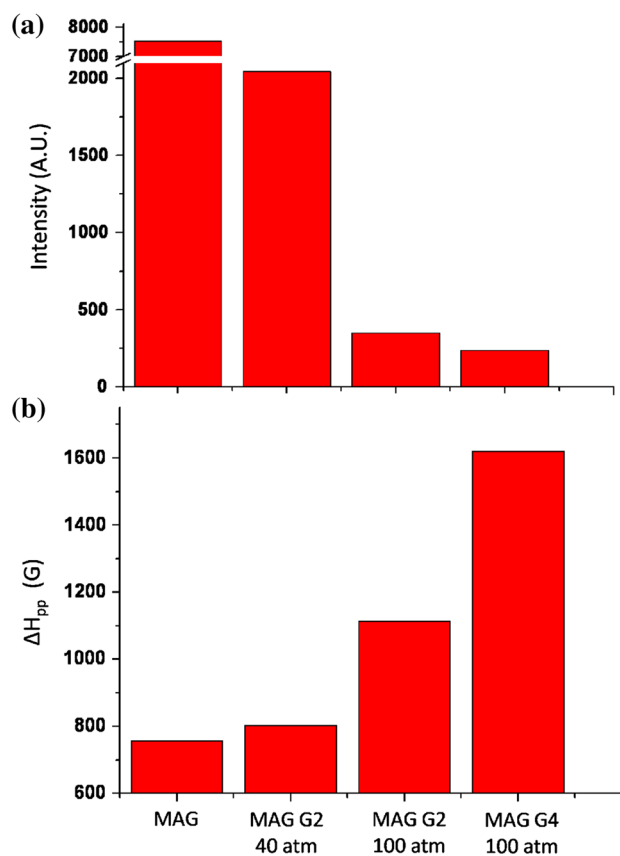

Fig. 7 a Intensity of the $g = 2.03$ line, estimated from double integration of the EPR spectra for MAG NPs into PAMAM-SAH dendrimers. b Linewidth (ΔH_{pp}) of the $g = 2.03$ line of the EPR spectra for MAG NPs into the PAMAM-SAH dendrimer

The linewidth (ΔH_{pp}) increases with synthesis pressure of nanostructured hybrid (Fig. 7b).

The distance between Fe^{3+} ions and dendrimer surface decreases with increasing pressure.

Two interaction mechanisms are possible: spin–lattice relaxation and spin–spin relaxation. Spin–lattice relaxation implies interaction between Fe^{3+} ions and dendrimer network. It is characterized by a relaxation time, T1. Spin–spin relaxation or cross relaxation refers to Fe^{3+}–Fe^{3+} interactions and is characterized by relaxation time T2. When both spin–lattice and spin–spin relaxations contribute to the EPR signal, the resonance linewidth (ΔH_{pp}) can be written as

$$\Delta H_{pp} \propto \frac{1}{T_1} + \frac{1}{T_2}. \tag{1}$$

From Eq. 1, we can tell that when $T_1 > T_2$, ΔH_{pp} depends primarily on spin–spin interactions.

The increase in ΔH_{pp} of the $g = 2.03$ absorption line could be explained by the increased dominance of clustering mechanism (spin–lattice interactions). The interactions of Fe^{3+} with the dendrimer surface may on one side separate the ions and diminish the spin–spin (Fe^{3+}–Fe^{3+})

interactions. Decreasing the spin–spin distance, which is the spin concentration, T_1 will become very short, and thus the spin–lattice relaxation will have a larger influence on the linewidth than spin–spin relaxation. On the other side, if the binding sites at the dendrimer surface (Fe^{3+} ions) are close to each other, the spin–spin interactions increase (T_2 will become very short), with a consequent decrease in the EPR intensity, while the linewidth increases [64].

Based on EPR results, it can be concluded that MAG is not entrapped in PAMAM structure and the interactions between organic and inorganic components take place at dendrimer's surface.

EPR results validated the MD simulation. Thus, the dendrimer generation is (i) proportionally related to the increase in the linewidth of EPR and (ii) inversely related to EPR intensity (Fig. 7a). A possible explanation based on the observations suggested by in silico investigation could be that at high pH, as the dendrimer generation increases, the dendrimer/MAG affinity raises consequently, due to the higher density of exposed succinic groups on the dendrimer outer surface. Hence, the probability of finding dendrimer/MAG bound states increases, and consequently the exchange narrowing due to the interactions between Fe^{3+} and Fe^{2+} is suppressed by the dendrimer coating over the MAG NPs.

Conclusions

In this work, a combined computational/experimental approach was employed to investigate structural characteristics of dendrimer/MAG hybrid nanostructures. Several generations of PAMAM and PAMAM-SAH were investigated by MD simulations in order to find a possible mechanism for the formation of hybrid structures. Computational results indicated that the interaction between PAMAM-SAHs and MAG is mainly driven by the electrostatic contribution, and the affinity of these dendrimers for MAG NPs is higher due to negatively charged succinic terminals. Morphostructural analysis of MAG NPs revealed the formation of crystallites with size range between 2 and 5 nm. In the presence of G2 PAMAM-SAH dendrimers, small crystallites of 6–15 nm were observed. In the case of G4 PAMAM-SAH dendrimers, the presence of MAG nanoparticles was proved by calculated interplanar distance (2.53 Å) and associated Miller index (311). In all types of hybrids, MAG crystallites with 3 nm in size have been highlighted. EPR results have shown that MAG is not entrapped in PAMAM structure and the interactions between organic and inorganic components take place at dendrimer's surface. This evidence has been also confirmed by calculating the dendrimer void volume from MD trajectories (Supporting Information section S1.3) following the protocol described in [65].

Further investigations aimed at precisely identifying the macromolecular organization of dendrimer/MAG clusters which may be considered as a fruitful future development of this work. Moreover, additional computational and experimental studies on dendrimer/MAG hybrids will extend the presented investigation to other dendrimer types and functionalization. From a computational point of view, also varying the size of the MAG NP may be an interesting extension of this study in order to understand how the binding mode is influenced by the ratio between dendrimer and NP size.

References

1. Schroeder A, Heller DA, Winslow MM, Dahlman JE, Pratt GW, Langer R et al (2012) Treating metastatic cancer with nanotechnology. Nat Rev Cancer 12:39–50
2. Darroudi M, Hakimi M, Goodarzi E, Oskuee RK (2014) Superparamagnetic iron oxide nanoparticles (SPIONs): green preparation, characterization and their cytotoxicity effects. Ceram Int 40:14641–14645
3. Popescu LM, Piticescu RM, Stoiciu M, Vasile E, Trusca R (2012) Investigation of thermal behaviour of hybrid nanostructures based on Fe_2O_3 and PAMAM dendrimers. J Therm Anal Calorim 110:357–362
4. Zhang DW, Chen CH, Zhang J, Ren F (2007) Fabrication of nanosized metallic copper by electrochemical milling process. J Mater Sci 43:1492–1496. doi:10.1007/s10853-007-2274-6
5. Lu S, Jiang Y, Wei C (2009) Preparation and characterization of EP/SiO_2 hybrid materials containing PEG flexible chain. J Mater Sci 44:4047–4055. doi:10.1007/s10853-009-3584-7
6. Popescu LM, Piticescu RM, Rusti CF, Maly M, Danani A, Kintzios S, Grinan MTV (2011) Preparation and characterization of new hybrid nanostructured thin films for biosensors design. Mater Lett 65:2032–2035
7. Tajabadi M, Khosroshahi ME, Bonakdar S (2013) An efficient method of SPION synthesis coated with third generation PAMAM dendrimer. Colloids Surf A 431:18–26
8. Shi X, Wang SH, Swanson SD, Ge S, Cao Z, Van Antwerp ME et al (2008) Dendrimer-functionalized shell-crosslinked iron oxide nanoparticles for in-vivo magnetic resonance imaging of tumors. Adv Mater 20:1671–1678
9. Jang WD, Kamruzzaman Selim KM, Lee CH, Kang IK (2009) Bioinspired application of dendrimers: from bio-mimicry to biomedical applications. Prog Polym Sci 34:1–23
10. Svenson S, Tomalia DA (2005) Dendrimers in biomedical applications-reflections on the field. Adv Drug Deliv Rev 57:2106–2129
11. Sekowski S, Buczkowski A, Palecz B, Gabryelak T (2011) Interaction of polyamidoamine (PAMAM) succinamic acid

dendrimers generation 4 with human serum albumin. Spectrochim Acta A 81:706–710

12. Strable E, Bulte JWM, Moskowitz B, Vivekanandan K, Allen M, Douglas T (2001) Synthesis and characterization of soluble iron oxide-dendrimer composites. Chem Mater 13:2201–2209

13. Pavan GM, Posocco P, Tagliabue A, Maly M, Malek A, Danani A et al (2010) PAMAM dendrimers for siRNA delivery: computational and experimental insights. Chemistry 16:7781–7795

14. Pavan GM, Monteagudo S, Guerra J, Carrion B, Ocana V, Rodriguez-Lopez J et al (2012) Role of generation, architecture, pH and ionic strength on successful siRNA delivery and transfection by hybrid PPV-PAMAM dendrimers. Curr Med Chem 19:4929–4941

15. Jensen LB, Pavan GM, Kasimova MR, Rutherford S, Danani A, Nielsen HM et al (2011) Elucidating the molecular mechanism of PAMAM-siRNA dendriplex self-assembly: effect of dendrimer charge density. Int J Pharm 416:410–418

16. Pavan GM, Albertazzi L, Danani A (2010) Ability to adapt: different generations of PAMAM dendrimers show different behaviors in binding siRNA. J Phys Chem B 114:2667–2675

17. Shen M, Shi X (2010) Dendrimer-based organic/inorganic hybrid nanoparticles in biomedical applications. Nanoscale 2:1596–1610

18. Shi X, Wang SH, Lee I, Shen M, Baker JR (2009) Comparison of the internalization of targeted dendrimers and dendrimer-entrapped gold nanoparticles into cancer cells. Biopolymers 91:936–942

19. Shi X, Lee I, Chen X, Shen M, Xiao S, Zhu M et al (2010) Influence of dendrimer surface charge on the bioactivity of 2-methoxyestradiol complexed with dendrimers. Soft Matter 6:2539–2545

20. Pan B, Cui D, Sheng Y, Ozkan C, Gao F, He R et al (2007) Dendrimer-modified magnetic nanoparticles enhance efficiency of gene delivery system. Cancer Res 67:8156–8163

21. Wang SH, Shi X, Van Antwerp M, Cao Z, Swanson SD, Bi X et al (2007) Dendrimer-functionalized iron oxide nanoparticles for specific targeting and imaging of cancer cells. Adv Funct Mater 17:3043–3050

22. Cheng Y (2012) Dendrimer-based drug delivery systems: from theory to practice, 1st edn. Wiley, Hoboken

23. Krzyminiewski R, Kubiak T, Dobosz B, Schroeder G, Kurczewska J (2014) EPR spectroscopy and imaging of TEMPO-labeled magnetite nanoparticles. Curr Appl Phys 14:798–804

24. Apicella A, Soncini M, Deriu MA, Natalello A, Bonanomi M, Dellasega D et al (2013) A hydrophobic gold surface triggers misfolding and aggregation of the amyloidogenic Josephin domain in monomeric form, while leaving the oligomers unaffected. PLoS One 8:e58794

25. Deriu MA, Grasso G, Licandro G, Danani A, Gallo D, Tuszynski JA et al (2014) Investigation of the Josephin domain protein-protein interaction by molecular dynamics. PLoS One 9:e108677

26. Paciello G, Acquaviva A, Ficarra E, Deriu MA, Macii E (2011) A molecular dynamics study of a miRNA: mRNA interaction. J Mol Model 17:2895–2906

27. Maingi V, Jain V, Bharatam PV, Maiti PK (2012) Dendrimer building toolkit: model building and characterization of various dendrimer architectures. J Comput Chem 33:1997–2011

28. Pavan GM, Mintzer MA, Simanek EE, Merkel OM, Kissel T, Danani A (2010) Computational insights into the interactions between DNA and siRNA with "rigid" and "flexible" triazine dendrimers. Biomacromolecules 11:721–730

29. Mandal T, Dasgupta C, Maiti PK (2013) Engineering gold nanoparticle interaction by PAMAM dendrimer. J Phys Chem C 117:13627–13636

30. Karatasos K, Posocco P, Laurini E, Pricl S (2012) Poly(amidoamine)-based dendrimer/siRNA complexation studied by computer simulations: effects of pH and generation on dendrimer structure and siRNA binding. Macromol Biosci 12:225–240

31. Maingi V, Kumar MVS, Maiti PK (2012) PAMAM dendrimer-drug interactions: effect of pH on the binding and release pattern. J Phys Chem B 116:4370–4376

32. Mukherjee G, Patra N, Barua P, Jayaram B (2011) A fast empirical GAFF compatible partial atomic charge assignment scheme for modeling interactions of small molecules with biomolecular targets. J Comput Chem 32:893–907

33. Sousa da Silva AW, Vranken WF (2012) ACPYPE—antechamber python parser interface. BMC Res Notes 5:367

34. Dupradeau FY, Pigache A, Zaffran T, Savineau C, Lelong R, Grivel N et al (2010) The R.E.D. tools: advances in RESP and ESP charge derivation and force field library building. Phys Chem Chem Phys 12:7821–7839

35. Cezard C, Vanquelef E, Pecher J, Sonnet P (2008) RESP charge derivation and force field topology database generation for complex bio-molecular systems and analogs. In: 236th ACS National Meeting

36. Vanquelef E, Simon S, Marquant G, Garcia E, Klimerak G, Delepine JC et al (2011) R.E.D. Server: a web service for deriving RESP and ESP charges and building force field libraries for new molecules and molecular fragments. Nucleic Acids Res 39:W511–W517

37. Bayly CI, Cieplak P, Cornell W, Kollman PA (1993) A well-behaved electrostatic potential based method using charge restraints for deriving atomic charges: the RESP model. J Phys Chem 97:10269–10280

38. Cygan RT, Liang JJ, Kalinichev AG (2004) Molecular models of hydroxide, oxyhydroxide, and clay phases and the development of a general force field. J Phys Chem B 108:1255–1266

39. Gale JD (1997) GULP: a computer program for the symmetry-adapted simulation of solids. J Chem Soc Faraday Trans 93:629–637

40. Gale JD, Rohl AL (2003) The general utility lattice program (GULP). Mol Simul 29:291–341

41. Gale J (2005) GULP: capabilities and prospects. Zeitschrift Für Krist 220:552–554

42. Rappé AK, Goddard WA III (1991) Charge equilibration for molecular dynamics simulations. J Phys Chem 95:3358–3363

43. Müller-Plathe F (2002) Coarse-graining in polymer simulation: from the atomistic to the mesoscopic scale and back. Chemical 3:754–769

44. Reith D, Pütz M, Müller-Plathe F (2003) Deriving effective mesoscale potentials from atomistic simulations. J Comput Chem 24:1624–1636

45. Cheng CP, Yang LW (2008) Coarse-grained models reveal functional dynamics–II. Molecular dynamics simulation at the coarse-grained level–theories and biological applications. Bioinform Biol Insights 2:171–185

46. Deriu MA, Shkurti A, Paciello G, Bidone TC, Morbiducci U, Ficarra E et al (2012) Multiscale modeling of cellular actin filaments: from atomistic molecular to coarse-grained dynamics. Proteins 80:1598–1609

47. Leroch S, Wendland M (2012) Simulation of forces between humid amorphous silica surfaces: a comparison of empirical atomistic force fields. J Phys Chem C 116:26247–26261

48. Bürger A, Magdans U, Gies H (2013) Adsorption of amino acids on the magnetite-(111)-surface: a force field study. J Mol Model 19:851–857

49. Jorgensen WL, Chandrasekhar J, Madura JD, Impey RW, Klein ML (1983) Comparison of simple potential functions for simulating liquid water. J Chem Phys 79:926

50. Hess B, Kutzner C, van der Spoel D, Lindahl E (2008) GROMACS 4: algorithms for highly efficient, load-balanced, and scalable molecular simulation. J Chem Theory Comput 4:435–447

51. Berendsen HJC, van der Spoel D, van Drunen R (1995) GROMACS: a message-passing parallel molecular dynamics implementation. Comput Phys Commun 91:43–56

52. Van Der Spoel D, Lindahl E, Hess B, Groenhof G, Mark AE, Berendsen HJC (2005) GROMACS: fast, flexible, and free. J Comput Chem 26:1701–1718

53. Humphrey W, Dalke A, Schulten K (1996) VMD: visual molecular dynamics. J Mol Graph 14(33–8):27–28

54. Eisenhaber F, Lijnzaad P, Argos P, Sander C, Scharf M (1995) The double cubic lattice method: efficient approaches to numerical integration of surface area and volume and to dot surface contouring of molecular assemblies. J Comput Chem 16:273–284

55. Kumari R, Kumar R, Lynn A (2014) g_mmpbsa–a GROMACS tool for high-throughput MM-PBSA calculations. J Chem Inf Model 54:1951–1962

56. Chaplin M (2015) Physical anomalies of water. http://www.lsbu.ac.uk/water/physical_anomalies.html. Accessed 29 May 2015

57. Goeke E (2011) Mineralogy: magnetite & hematite—minerals of the week #2. https://lifeinplanelight.wordpress.com/2011/02/28/mineralogy-magnetite-hematite-minerals-of-the-week-2/. Accessed 19 May 2015

58. Chaplin M (2015) Water ionization, the ionic product (Kw) of water and pH. http://www.lsbu.ac.uk/water/water_dissociation.html. Accessed 19 May 2015

59. Imreh I (1987) Geochimie. Editura Dacia, Cluj-Napoca

60. Matthews A (1976) Magnetite formation by reduction of hematite with iron under hydrothermal conditions. Am Mineral 61:927–932

61. Chaplin M (2015) Material anomalies of water. http://www.lsbu.ac.uk/water/material_anomalies.html. Accessed 19 May 2015

62. Castner T, Newell GS, Holton WC, Slichter CP (1960) Note on the paramagnetic resonance of iron in glass. J Chem Phys 32:668

63. Abragam A, Bleaney B (1970) Electron paramagnetic resonance of transition ions. Oxford University Press, Oxford

64. Barklie RC, Collins M, Silva SRP (2000) EPR linewidth variation, spin relaxation times, and exchange in amorphous hydrogenated carbon. Phys Rev B 61:3546–3554

65. Maiti PK, Çagın T, Wang G, Goddard WA (2004) Structure of PAMAM dendrimers: generations 1 through 11. Macromolecules 37:6236–6254